EES Batteries

PAPER

View Article Online
View Journal | View Issue

Cite this: *EES Batteries*, 2026, **2**, 562

Perinone isomerism effect on proton insertion chemistry

Qing Lang,[a] Jian Zhang,[a] Ziqi Tian,[a] Qi Fan,[b] Kun Liang,[b] Yunan Wang,[a] Evgenia Dmitrieva,[c] Liang Chen,[a] Congxue Liu,*[d] Mingchao Wang,[d] Maryam AlNahyan,[e] Panče Naumov *[f,g,h,i] and Gang Wang *[a]

Aqueous proton batteries (APBs) have attracted increasing attention due to their high safety and fast kinetics derived from proton insertion chemistry. Redox-active organic compounds with tunable molecular structures are promising electrode materials for APBs, yet their implementation remains limited by suboptimal cycling stability owing to dissolution of intermediates and structural degradation. Here, we introduce an unexplored concept of exploiting geometric isomerism to tailor structure–property relationships in proton storage. Using highly π-conjugated *cis*- and *trans*-perinone isomers as the model system, we reveal that the spatial arrangement of carbonyl groups significantly influences proton insertion processes, overpotential, kinetics, and stability. Proton insertion is confirmed to proceed *via* a staging mechanism involving both bare and hydrated protons, *i.e.* H^+ and $H^+{\cdot}(H_2O)_n$, respectively. Co-insertion of water molecules is comparatively more into the *trans*-isomer relative to the *cis*-isomer, resulting in irreversible lattice distortion and inferior potential stability of the former. The *cis*-isomer delivers exceptional cycling performance with 100% capacity retention after 8000 cycles, exceeding state-of-the-art organic proton-storage materials. This work highlights the crucial role of molecular geometry in dictating electrochemical behavior and offers valuable insights for developing high-performance, practically useful organic rechargeable batteries.

Received 24th December 2025,
Accepted 26th February 2026

DOI: 10.1039/d5eb00242g

rsc.li/EESBatteries

Broader context

Aqueous proton batteries (APBs) have emerged as a promising candidate due to the minimal ionic radius and mass and the well-established Grotthuss mechanism of the H^+ mobility. Redox-active organic compounds as efficient proton hosts have recently attracted much attention due to their structure flexibility. However, their implementation remains limited by suboptimal cycling stability owing to dissolution of intermediates and structural degradation, although various physical coating or chemical modification strategies have been proposed. There is an urgent need to explore new paradigms for structural regulation from the molecular design level, aiming to fundamentally improve the intrinsic stability. Here, we introduce an unexplored concept of exploiting geometric isomerism to tailor structure–property relationships in proton storage. Using highly π-conjugated *cis*- and *trans*-perinone isomers as the model system, it is confirmed that spatial arrangement of carbonyl groups significantly influences proton insertion processes, overpotential, kinetics, and stability. The highly stable organic small molecule *cis*-perinone stands out with no capacity attenuation during long-term cycling. This work highlights the crucial role of molecular geometry in dictating electrochemical behavior and offers valuable insights for developing high-performance, practically useful organic rechargeable batteries.

[a]*Zhejiang Key Laboratory of Advanced Fuel Cells and Electrolyzers Technology, Materials Tech Laboratory for Hydrogen & Energy Storage, Ningbo Institute of Materials Technology and Engineering (NIMTE) of the Chinese Academy of Sciences (CAS), Ningbo 315201, P. R. China. E-mail: gang.wang@nimte.ac.cn*
[b]*Zhejiang Key Laboratory of Data-Driven High-Safety Energy Materials and Applications, Ningbo Institute of Materials Technology and Engineering of the Chinese Academy of Sciences, Ningbo 315201, China*
[c]*Leibniz Institute for Solid State and Materials Research Dresden (IFW), Helmholtzstraße 20, 01069 Dresden, Germany*
[d]*Guangdong Provincial Key Laboratory of Nano-Micro Materials Research & State Key Laboratory of Advanced Waterproof Materials, School of Advanced Materials, Peking University, Shenzhen Graduate School, Shenzhen 518055, China. E-mail: liucongxue@pku.edu.cn*
[e]*Division of Engineering, New York University Abu Dhabi, POB 129188, Abu Dhabi, United Arab Emirates*
[f]*Smart Materials Lab, New York University Abu Dhabi, PO Box 129188, Abu Dhabi, United Arab Emirates*
[g]*Center for Smart Engineering Materials, New York University Abu Dhabi, PO Box 129188, Abu Dhabi, United Arab Emirates*
[h]*Research Center for Environment and Materials, Macedonian Academy of Sciences and Arts, Bul. Krste Misirkov 2, MK-1000 Skopje, Macedonia*
[i]*Molecular Design Institute, Department of Chemistry, New York University, 100 Washington Square East, New York, NY 10003, USA. E-mail: pance.naumov@nyu.edu*

Introduction

With the ever-increasing demand for safe and low-cost energy storage technologies, aqueous rechargeable batteries have seen an impressive development.[1–3] Among them, aqueous proton batteries (APBs) are distinct as one of the most powerful quick-(dis)charge energy storage devices, due to the minimal ionic radius and mass and the well-established Grotthuss mechanism of the H^+ mobility.[4–6] In the continuing attempts to capitalize on the proton insertion chemistry, both inorganic and organic materials have been explored.[7–9] Specifically, redox-active organic materials are thought to hold great promise based on their abundance, low toxicity and structural flexibility.[10–13] A variety of organic materials have been developed for efficient proton storage to date,[14–24] including carbonyl-functionalized compounds,[25–27] most notably, the high-capacity electrode material pyrene-4,5,9,10-tetraone (PTO, 376 mAh g^{-1}), tetramethyl-benzoquinone (TMBQ, 300 mAh g^{-1}), and the low-potential material anthraquinone (−0.16 V *vs.* Ag/AgCl).[28–30] Unfortunately, most organic molecules are prone to degradation in cycling operations and have low conductivity, requiring novel organic electrode materials with advanced electrochemical properties.

Polycyclic perinone, which is a commonly used industrial pigment, consists of a linearly fused naphthalene and imidazole rings (Fig. 1a).[31–34] The extended π-delocalization and expanded planar arylene structure endow perinone with both chemical and thermal stability, but also account for the narrow highest occupied molecular orbital (HOMO)–lowest unoccupied molecular orbital (LUMO) gap, which facilitates charge transport.[35] In our previous work, perinone-based poly (benzimidazobenzophenanthroline) (BBL)-type covalent organic frameworks (COFs) were found to have high charge mobilities and fast proton storage capability.[36,37] BBL and its phenazine analogue are proven to be stable electrode materials in APBs;[38,39] however, the *cis*-/*trans*-mixed perinone structure in the reported BBL or COFs poses challenges with exerting control over the spatial carbonyl group arrangement, and the behavior of these isomeric units during the redox reactions on the overall electrochemical performance remains unclear. Small intramolecular changes are expected to affect the electrochemical behavior,[40,41] and in that context organic isomers are becoming increasingly relevant.[42–45]

Herein, we take perinone as the first example of *trans*/*cis*-isomerism for proton storage and we report a disparate effect of the disposition of its carbonyl groups on its electrochemical behavior. *trans*-Isomer **2** suffers from deteriorating potential upon cycling and a large overpotential, while the *cis*-isomer **1** remains stable both in structure and electrochemical performance. The isomerism effect governs the evolution of distinct microscopic crystal structures and affects the ion intercalation volume, ultimately leading to divergent macroscopic performance. *In situ* electrochemical quartz crystal microbalance (EQCM), *ex situ* X-ray diffraction (XRD) and crystallography reveal that the large hydrated proton species ($H^+ \cdot (H_2O)_n$) inserted in **2** leads to irreversible spacing and lattice expansion, causing deteriorating performance. Impressively, **1** demonstrates a capacity retention of 100% after 8000 cycles, which is superior over state-of-the-art organic proton hosts. When coupled with the MnO_2 or activated carbon (AC) cathode, both cells exhibited high cycling stability without capacity fading.

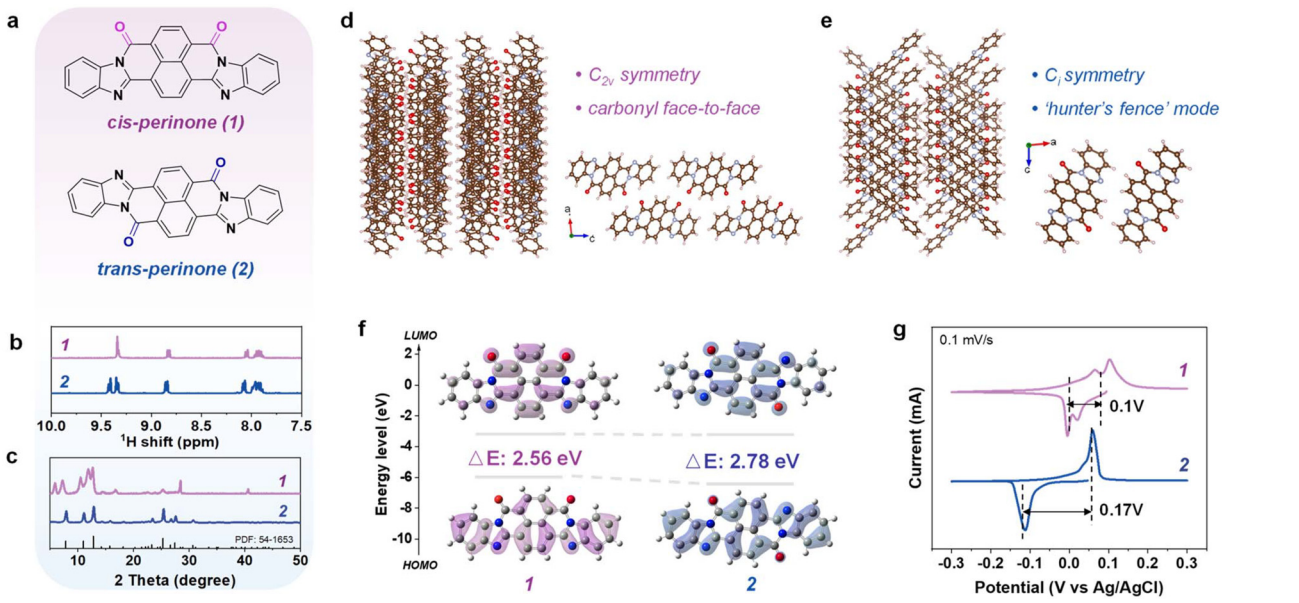

Fig. 1 Structural characterization of the perinone isomers. (a) Chemical structures of compounds **1** and **2**. (b) ^{1}H NMR spectra of the two isomers. (c) Powder XRD patterns of the two isomers. (d) Perspective view of the unit cell of **1** in its crystal (refcode of the data retrieved from CCDC: 1872270). (e) Perspective view of the unit cell of **2** in its crystal (refcode of the data retrieved from CCDC: 214992). (f) Calculated HOMO/LUMO energy levels and band gaps of the two isomers. (g) CV curves (1st cycle) of **1** and **2** at a scan rate of 0.1 mV s^{-1}.

Results and discussion

Structures and isomerism

The perinone isomers (Fig. 1a) were prepared by condensation, followed by separation (Scheme S1).[36] A solid mixture of *cis*-perinone (**1**) and *trans*-perinone (**2**) was synthesized first and had a *cis*-to-*trans* ratio of 43 : 57. Following a reflux in an alkaline solution, a brilliant orange solid of the *trans*-isomer (**2**) precipitated first during cooling, while the blueish-red *cis*-perinone (**1**) was obtained from the filtrate *via* acid treatment. The axisymmetric structure of **1** gives rise to a doublet ^{1}H peak in the nuclear magnetic resonance (NMR) spectra at 9.3 ppm, while **2** has a doublet of doublet proton signal (Fig. 1b and Fig. S1–S3). The powder XRD patterns indicate different crystal structures of the two isomers (Fig. 1c). Modelling confirmed that **1** exhibits C_{2v} molecular symmetry and is arranged in a 'carbonyl face-to-face' style along the *b* axis, while **2** presents a C_i-symmetry in a 'hunter's fence' mode (Fig. 1d, e and Table S1).[46–48] Solids of the two isomers were also charactered by Raman analysis and scanning electron microscopy (SEM) (Fig. S4 and S5) and both show a cudgel-shaped morphology, with **2** having a higher aspect ratio. The highest occupied molecular orbital (HOMO) and the lowest unoccupied molecular orbital (LUMO) were further evaluated by density functional theory (DFT) calculations to compare the electronic structures of two isomers (Fig. 1f). The narrower HOMO–LUMO gap (2.56 eV) of **1** indicates its superior charge transport efficiency compared to **2** (2.78 eV), 1,4,5,8-naphthaldiimide (NTCDI, 3.52 eV), PTO (3.34 eV), and diquinoxalino [2,3-*a*:2′,3′-*c*] phenazine (HATN, 3.60 eV), among other compounds (Table S2).

Electrochemical characterization

To evaluate the redox activity of the isomers, cyclic voltammetry (CV) was initially conducted in 0.5 M H_2SO_4 as the electrolyte in a three-electrode system with an Ag/AgCl reference electrode and an activated carbon counter electrode (Fig. S6a). It was found that both isomers were redox active (Fig. 1g), while the peak separation of **1** was about 100 mV and much lower than 175 mV for **2**. The average redox potential of two isomers was 0.05 V for **1** and −0.08 V for **2** (*vs.* Ag/AgCl). The solid-solution mixture before separation of the isomers resembled **2** in the CV shape and had an average potential of 0 V and a medium polarization of 125 mV (Fig. S7).

In a potential window of −0.3 V–0.3 V, galvanostatic measurements of **1** and **2** were carried out at 0.1 A g^{-1} within the three-electrode cells. The working electrodes were prepared by mixing perinone, carbon black and polytetrafluoroethylene in an optimized mass ratio of 70 : 20 : 10 on a Ti foil (Fig. S8). In the first cycle, **1** showed a discharge plateau at −0.05 V and a charge plateau at 0.05 V (Fig. 2a), affording an overpotential of ∼0.1 V. **2** exhibited a larger overpotential of ∼0.18 V, with a relatively flat discharge plateau at −0.13 V and a charge plateau at 0.05 V (Fig. 2c). The plateau indicates phase transitions of **1** and **2**. There exist two pairs of sharp redox peaks for **1** and only one pair of peaks for **2** on the first-cycle dQ/dV curve (Fig. 2b and d), agreeing well with CV results (Fig. 1g) and corresponding to a two-step reaction and a one-step reaction, respectively.

Both **1** and **2** exhibit lower discharge potentials and higher overpotentials in the first cycle than others (Fig. S9) that is related to charge carriers and will be discussed in the following section. After the initial several cycles, **1** showed excellent cycling stability with nearly overlapped charge–discharge profiles within 50 cycles (Fig. 2a and b). In contrast to **1**, the charge–discharge curves of **2** varied significantly, along with transition from one charge–discharge platform to three platforms (Fig. 2c and d). Such potential shift of **2** was not limited to sulfuric acid electrolyte and was also observed with 1 M HCl and 1 M H_3PO_4 (Fig. S10). Moreover, **1** exhibited much lower overpotentials than **2** during the whole cycling process (Fig. 2e and S11). These results indicate that *cis–trans* isomerism affects the electrochemical behavior of the perinone electrode. The performance of the nascent mixture of isomers as a control sample was inferior to that of **1** in stability even though the potential shift was less than that of **2** (Fig. S12).

Both **1** and **2** exhibited a high reversible capacity of 120 mAh g^{-1} and over 99.3% coulombic efficiency (CE) at a low current density of 0.1 A g^{-1}, corresponding to 93% active site utilization based on its theoretical capacity of two-electron transfer (130 mAh g^{-1}). Note that some proton hosts suffer from inevitable dissolution; stable cycling was not achievable at low rate (Fig. S13).[10] Instead, high current measurements were always adopted to shorten the whole test period. Remarkably, the capacity retention of **1** and **2** was 100% after 100 cycles at 0.1 A g^{-1} (Fig. S14), ruling out any materials loss due to dissolution (Fig. S15). The potential shift of **2** did not influence the utilization of active sites and thus its redox activity.

In terms of rate performance, **1** delivered a high specific capacity of 90 mAh g^{-1} at 10 A g^{-1}, maintaining 75% capacity at 0.1 A g^{-1}, while **2** retained a capacity of 70 mAh g^{-1} at the same rate (Fig. S16 and 17). More importantly, there was only little polarization enhancement for **1** with the augment of current density from 0.1 to 10 A g^{-1}, in sharp contrast to the double overpotential (from 120 mV to 225 mV) observed for **2**. The electrochemical kinetics of the perinone isomers were further studied by CV at different scan rates. The calculated *b* values of dominant peaks are 0.69 and 0.66 for **1** and 0.58 and 0.55 for **2**, implying slightly better kinetics of **1** over **2** (Fig. S18). Encouraged by the high electrochemical performance of the *cis*-isomer **1**, galvanostatic charge/discharge (GCD) tests were further carried out under high mass loading. Increasing the areal loading from 1.7 mg cm^{-2} to 27.6 mg cm^{-2}, **1** electrode could output a stable areal capacity of 3.4 mAh cm^{-2} at 0.1 A g^{-1} (Fig. 2f), corresponding to a specific capacity of 123 mAh g^{-1}. Surprisingly, an increase in the areal mass loading of **1** by a factor of over ten times only increased the overpotential from 60 to 91 mV (Fig. 2g). Even at high mass loading, **1** delivered a high capacity of 68 mAh g^{-1} at 1 A g^{-1}, highlighting the kinetic advantage (Fig. S19). All the results indicated excellent scale up capability of **1** electrode for practical implementation.

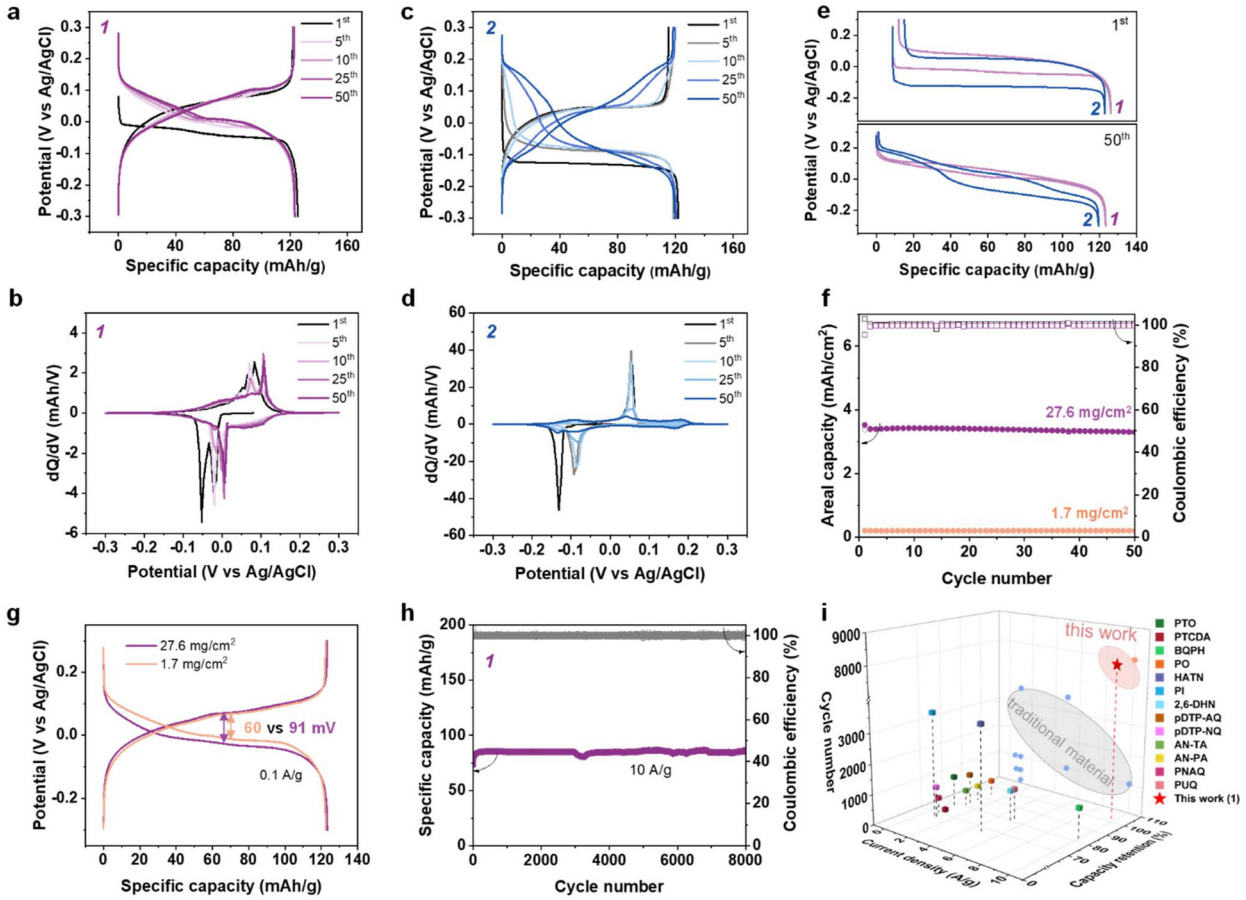

Fig. 2 Electrochemical performances of **1** and **2**. (a) Charge–discharge curves for different cycles of **1** (1st, 5th, 10th, 25th, 50th). (b) d*Q*/d*V* curves of **1** at 0.1 A g^{-1}. (c) Charge–discharge curves for different cycles of **2** (1st, 5th, 10th, 25th, 50th). (d) The d*Q*/d*V* curves of **2** at 0.1 A g^{-1}. (e) Comparison of overpotentials for **1** and **2** at the 1st and 50th cycle. (f) Cycling performance of the electrode of **1** under different areal mass loadings (1.7 and 27.6 mg cm^{-2}) at 0.1 A g^{-1}. (g) Typical charge–discharge curves of **1** under different areal mass loadings. (h) Cycling performance of **1** at 10 A g^{-1}. (i) Comparison of the cycling stability of **1** with other organic electrode materials for proton storage.

The long-term cycling stability of **1** electrode was analysed at 10 A g^{-1}. As shown in Fig. 2h, after 8000 cycles, the capacity retention of **1** electrode was as high as 100%. The Raman, FTIR and SEM-EDX analyses suggested that the chemical structure and morphology of **1** are well preserved after long-term cycling (Fig. S20–22). Notably, the cycling stability of **1** surpassed state-of-the-art organic electrodes for proton storage (Fig. 2h and Table S3).[27,49–56] This favorable electrochemical stability of **1** can be attributed to the high planarity, highly π-conjugated structures and strong π–π intermolecular interactions in its structure, which were reflected in the density functional theory (DFT) models (Fig. S23).[57,58] The *cis*-isomer of **1** has a low molecular planarity parameter (MPP) value of 0.001 and balanced electrostatic potential (ESP), which are expected to reduce the molecular dissolution. Furthermore, the π electrons of **1** are well delocalized across the molecule and strong π–π interactions exist between the layers, both of which are stabilizing factors during the protonation/deprotonation process. The model for compound **2** (Fig. S24) is quite similar to that for **1**, which explains the absence of capacity attenuation of **2** and active material loss during cycling, despite the unfavorable potential shift.

Mass and charge transfer processes

Charge carriers have a significant effect on the electrochemical reaction. Both bare protons (H^+)[14] and hydrated protons ($H^+ \cdot (H_2O)_n$)[27] have been reported as charge carriers in APBs. *In situ* electrochemical quartz crystal microbalance (EQCM)[59] is an effective yet non-destructive tool to directly monitor the charge species that interact with or are inserted into the active material in a real electrochemical reaction and provides electrochemical and gravimetric information in real time. To identify the mass change of the perinone electrodes, an *in situ* EQCM[60–62] measurement was carried out during cyclic voltammetry tests at 5 mV s^{-1}. The blank gold sensor shows a significant side reaction in 0.5 M H_2SO_4 below −0.25 V *vs.* Ag/AgCl, although there are few effects on the frequency (Fig. S25). Therefore, the CV tests were carried out within a limited potential window of −0.2 V–0.3 V. The frequency data directly reflect the mass change. In the first reduction scan of the CV test, sig-

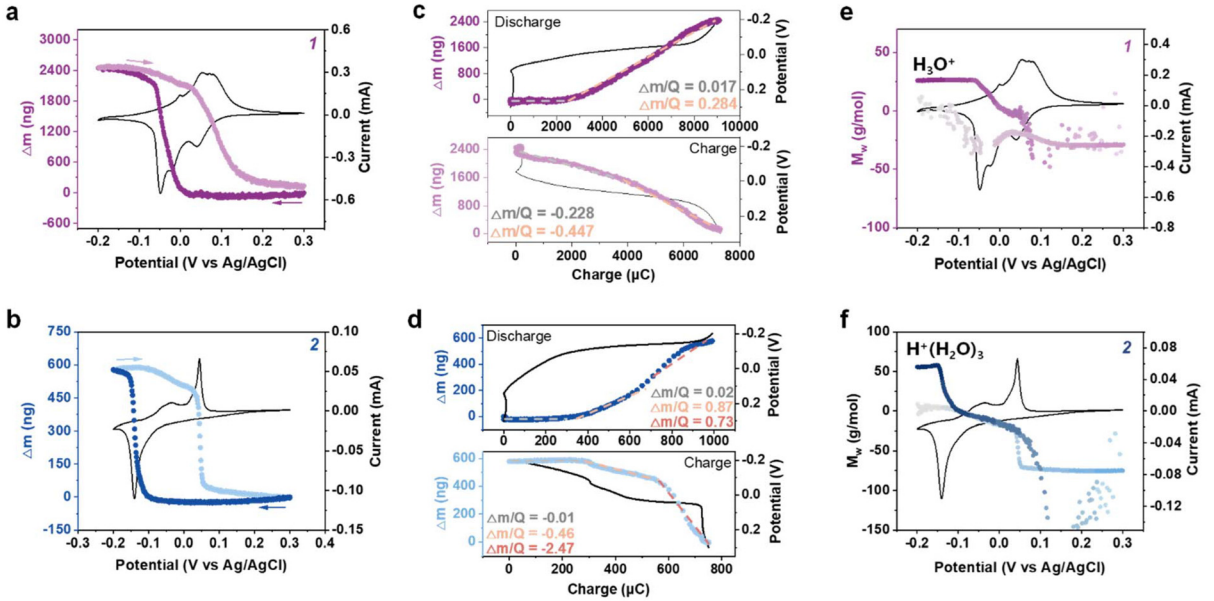

Fig. 3 Real-time CV with EQCM for the two isomers. (a) Mass profiles for **1** during the CV test; (b) mass profiles for **2** during the CV test; (c) mass change *vs.* charge during polarization for **1**; (d) mass change *vs.* charge during polarization for **2**; (e) M_w of the transferred species during CV for **1**; (f) M_w of the transferred species during CV for **2**.

nificant mass gain was observed due to insertion of proton charge carriers into electrodes of **1** and **2** (Fig. S26), while oxidation scan led to mass loss of the electrode. A large mass gap was noticed and implies an irreversibly trapped mass. More water molecules associated with H^+ were found to be inserted in the first cycle compared to the subsequent cycles (Fig. S27), resulting in an energy penalty and a low discharge potential in the first cycle (Fig. 2a and b). In the subsequent CV tests, the mass gap turned lower until mass equilibrium was reached (Fig. 3a and b).

At mass equilibrium of the electrode, the mass and charge profiles were plotted together to explore the essence of mixed electron-ion-water transfer in detail. The slope of each region ($\Delta m/Q$) in profiles reflects mass transmission during the redox process. Results suggest that the profiles for **1** can be divided into two mass transfer stages, corresponding to the $\Delta m/Q$ values of 0.017 mg C^{-1}, 0.284 mg C^{-1} for discharge, and −0.228 mg C^{-1}, −0.447 mg C^{-1} for the charge process, respectively (Fig. 3c). Three stages were observed for **2**, in which experimental $\Delta m/Q$ values with protons as the dopant were 0.02 mg C^{-1}, 0.87 mg C^{-1} and 0.73 mg C^{-1} for discharge and −0.01 mg C^{-1}, −0.46 mg C^{-1}, −2.47 mg C^{-1} for the charge process (Fig. 3d). For the theoretical $\Delta m/Q$ (0.01 mg C^{-1}) of bare H^+, the corresponding charge carriers determined for **1** are H^+–$H^+{\cdot}(H_2O)_{1.5}$ during discharge and $H^+{\cdot}(H_2O)_{1.2}$–$H^+{\cdot}(H_2O)_{2.4}$ during charge. For **2**, they were H^+–$H^+{\cdot}(H_2O)_{4.6}$–$H^+{\cdot}(H_2O)_{3.9}$ and H^+–$H^+{\cdot}(H_2O)_{2.5}$–$H^+{\cdot}(H_2O)_{13}$. For better understanding, the apparent molecular weight (M_w) of the transferred species was also calculated from Faraday's law to quantify the average number of transferred water molecules (Fig. 3e and f). Overall, the transferred water molecules ($H^+{\cdot}(H_2O)_n$) were 1.24/1.32 and 3.07/3.1 during charge–discharge for **1** and **2** electrodes, indicating that more water molecules were co-inserted into **2** than **1**.

Proton storage mechanism

Given the high electrochemical stability of the *cis*-isomer, we next investigated the energy storage mechanism of **1**. Electron paramagnetic resonance (EPR)/UV-vis-NIR spectroelectrochemistry (SEC) were carried out by collecting time-resolved and *in situ* electrochemical and spectroscopic information (Fig. S28). Upon reduction, the EPR spectra showed a single signal with a *g* value of 2.0033 and a line width of *ca.* 1 Gauss (Fig. 4a), suggesting the formation of the radical anion $\mathbf{1}^{\bullet-}$ (inset of Fig. 4b). The EPR signal intensity significantly increased along with the reduction and reached its maximum at the reduction peak current (Fig. 4b), revealing complete conversion of **1** to $\mathbf{1}^{\bullet-}$ (first-step reduction). Then the EPR signal gradually decreased till full reduction, where further electron transfer changed $\mathbf{1}^{\bullet-}$ to the EPR-silent dianion $\mathbf{1}^{2-}$ (second-step reduction). The closed-shell $\mathbf{1}^{2-}$ rather than the open-shell $\mathbf{1}^{2(\bullet-)}$ is proposed as the most plausible reduction product of **1**. A similar intensity change of the EPR signal was noticed during the oxidation scan, which indicates that a two-step reaction ($\mathbf{1} \leftrightarrow \mathbf{1}^{\bullet-} \leftrightarrow \mathbf{1}^{2-}$) with even number of electrons transferred in each step is involved during the redox process of perinone. The detailed UV-vis-NIR spectra of perinone are provided in Fig. S28, which shows the evolution of absorption bands at 754 nm and 1570 nm due to the formation of the radical anion of **1**. Unfortunately, EPR/UV-vis-NIR SEC tests on the *trans*-isomer sample were not feasible, and thus *ex situ* EPR measurements were performed instead (Fig. S29). No

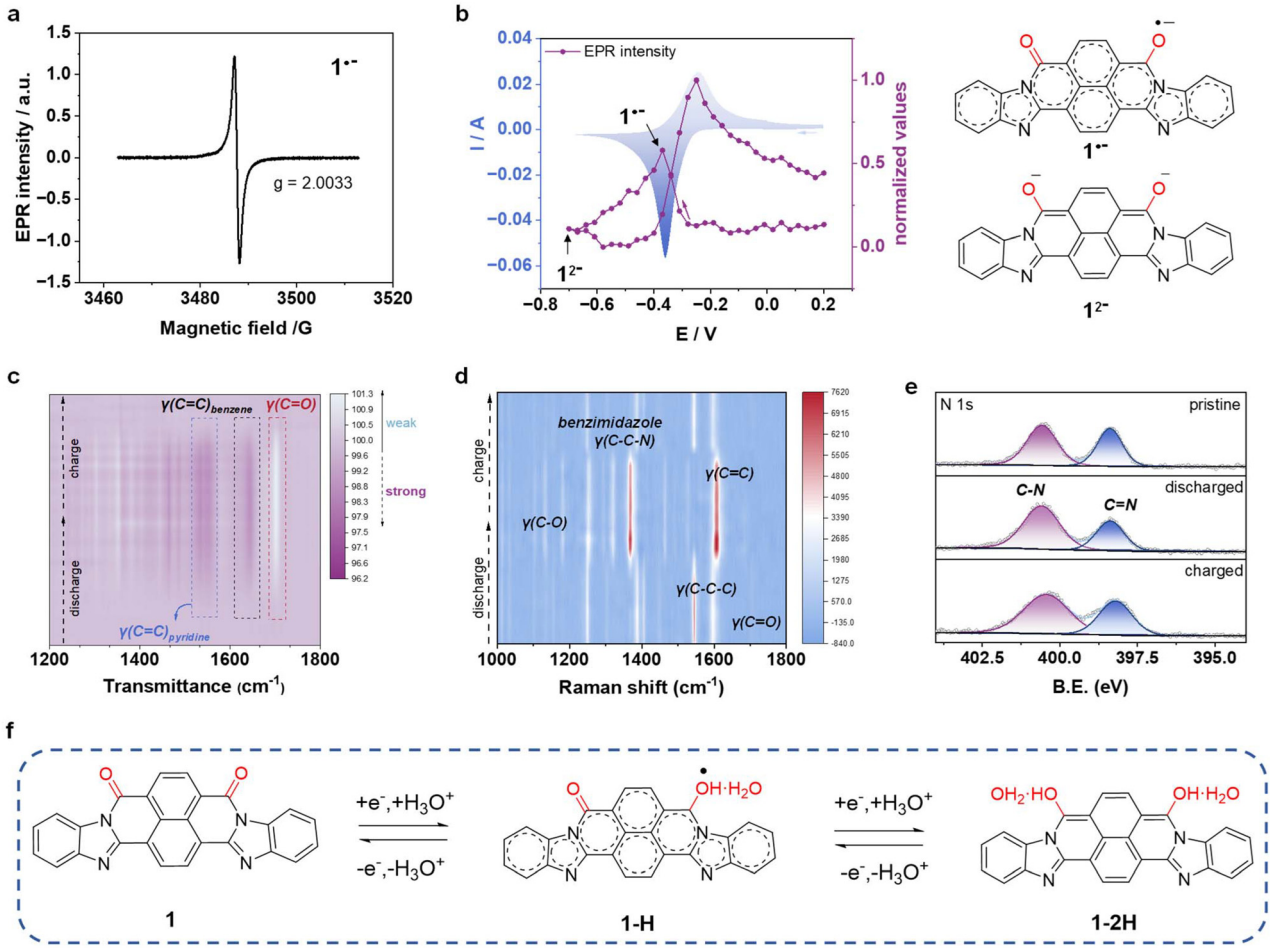

Fig. 4 The proton storage mechanism of **1**. (a) EPR spectrum of $\mathbf{1}^{\bullet-}$; (b) *in situ* EPR test of 1 during CV (2nd cycle); the inset shows the chemical structures of $\mathbf{1}^{\bullet-}$ and $\mathbf{1}^{2-}$; (c) *in situ* FTIR test (1st cycle); (d) *in situ* Raman spectroscopy (1st cycle); (e) XPS N 1s spectra for **1** electrode in the pristine, fully discharged and charged states; (f) the proposed redox mechanism of **1**.

detectable EPR signal was observed during the whole discharge–charge cycle for **2**, in contrast to the strong EPR signal that appeared in the intermediate progress of discharging (B) and charging (D) for **1**.

Subsequently, *in situ* FTIR spectroscopy was used to track the structure evolution of **1** during the electrochemical reactions (Fig. 4c and S30; the colorless region represents a decrease in intensity and the purple region represents an increase of band intensity). During discharging, the band from the symmetric C═O stretching at about 1700 cm^{-1} gradually disappeared and a new broad band from the –OH stretching emerged at 3390 cm^{-1}, indicating the participation of the C═O groups in the redox reaction (Fig. S31). The bands from the C═C stretching of the pyridine rings at 1550 cm^{-1} and the C═C benzene ring stretching band at 1650 cm^{-1} were both enhanced after the protonation due to the formation of the quinone-vinyl moiety. Once charging, the peak of C═O groups reemerged along with weakened C═C peaks. *In situ* Raman and *ex situ* X-ray photoelectron spectroscopy (XPS) analyses were further carried out to check whether the C═N bonds contributed to the redox reactions. As shown in Fig. 4c, reduction of the band due to the C═O (1700 cm^{-1}) stretching and enhancement of the band due to the C–O stretching (1180 cm^{-1}) are apparent in the Raman spectra (Fig. S32 and S33). The intensity of the strong band at 1595 cm^{-1} representing the C–C–C stretching of naphthalene[63] was reduced, while the C═C (1609 cm^{-1}) stretching was enhanced upon discharging, in line with the FTIR spectra. The characteristic benzimidazole modes γ(C–C–C) and γ(C–C–N)[64] at 1380–1400 cm^{-1} underwent a red-shift, accompanied by an increase in intensity, suggesting that the integrity of the benzimidazole structure was retained during the redox processes. DFT calculations confirmed that the peak shift can be attributed to changes in the conjugation of the benzimidazole fragment in the protonated structures (Fig. S34). In the XPS N 1s spectra, the C═N (398.2 eV) and C–N (400.5 eV) peaks remained unchanged in the pristine, fully discharged and charged states (Fig. 4d), a result which ruled out contribution from the C═N groups. Moreover, the DFT calculations also confirm that C═N sites exhibit much lower reduction potential based on decreased Gibbs free energy (Fig. S35). Consequently, we infer that the C═O groups, rather than the C═N groups, are the redox active

site for **1** and two protonated perinone structures are entailed through a two-step one-electron transfer pathway (Fig. 4f).

Structural changes

To explore the effect of the proton insertion on the crystal structure of the perinone isomers, *ex situ* XRD analysis was first performed on pristine (A), fully discharged (B) and fully charged (C) electrodes. Upon discharge, the diffraction peaks corresponding to (00$\bar{2}$), (100), ($\bar{1}$02), (102), (200) at the respective angles of 5.9°, 7.2°, 10.5°, 11.9°, 12.7° for **1** disappeared, and two new peaks at 5.2° and 9.8° emerged (Fig. 5a).[46] For **2**, the (100), (002), and (102) peaks at 7.8, 11.0 and 12.9° evolved into three peaks at 5.9°, 11.4°, and 12.3° (Fig. 5b).[46] These results indicate significant changes in the crystal structures of **1** and **2** after insertion of hydrated protons, a process that was also accompanied by a visible color change of the electrodes. Upon charging, the structures of both isomers recovered to their initial states.

Based on the XRD patterns of fully discharged electrodes, crystallographic data refinement calculations were then conducted to elucidate the possible protonated structures of **1** and **2**. For simplicity, the calculations were performed by associating one C═O with one H_3O^+ for **1** and one C═O with one $H^+{\cdot}(H_2O)_3$ for **2**. The simulated models reproduced the experimental results well and returned similar intensities (Fig. S36 and Table S4). Correspondingly, we attribute the XRD peaks at 5.2° and 9.8° of **1** to the (01$\bar{1}$) and (02$\bar{2}$) planes and the peaks at 5.9°, 11.4°, and 12.3° of **2** to the (100), (002) and (200) planes. Fig. 5c depicts the fully relaxed structure of protonated **1**, where a unique hydrogen-bonding network connecting hydroxy–water–hydroxyl groups is formed. The strong hydrogen-bonding interactions make the protonated **1** more compact, which is evident by the shortened O-to-O distance from 7.01 Å to 6.61 Å. The 'carbonyl face-to face' stacking mode of **1** facilitates the embedding of the water molecule only into the carbonyl-rich rather than in the carbonyl-free

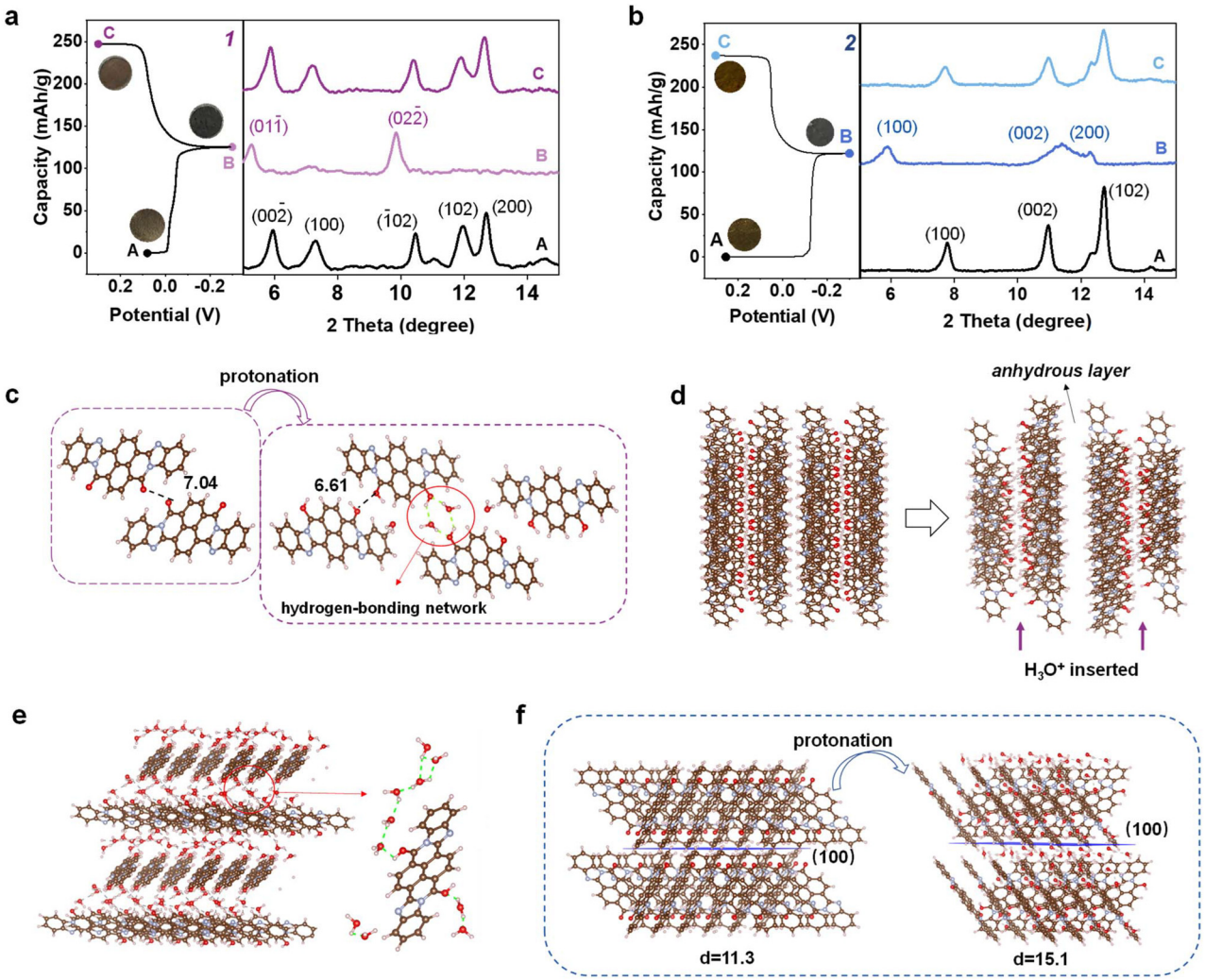

Fig. 5 Crystal structure perturbation of the two isomers. (a) *Ex situ* XRD patterns of the pristine, fully discharged, and fully charged electrodes of **1**; (b) *ex situ* XRD patterns of the pristine, fully discharged, and fully charged **2** electrodes; (c) structural models of protonated **1**; (d) packing mode of pristine **1** and protonated **1**; (e) structural models of protonated **2**; (f) packing changes of pristine **2** and protonated **2**.

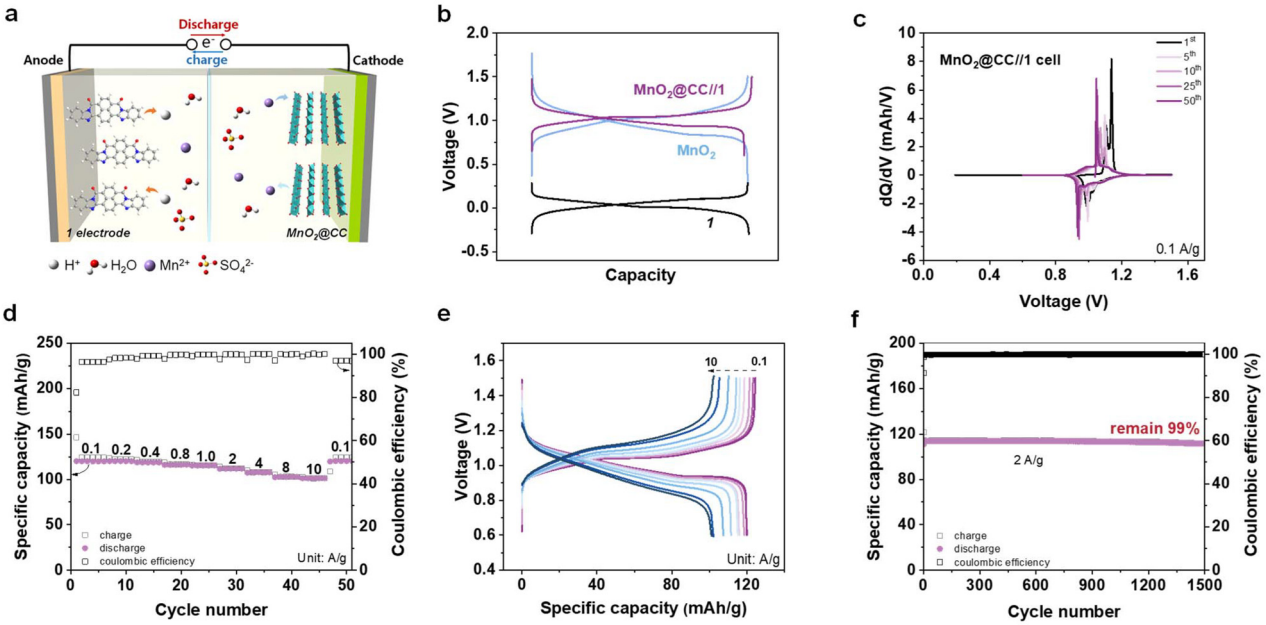

Fig. 6 Electrochemical performance of the MnO_2@CC//**1** full cell. (a) Battery configuration. (b) GCD curves of the **1** anode, MnO_2 cathode and MnO_2@CC//**1** battery. (c) The dQ/dV curves of the MnO_2@CC//**1** battery at 0.1 A g^{-1}. (d) Rate performance at different current densities of the MnO_2@CC//**1** battery. (e) GCD curves of the MnO_2@CC//**1** battery at different current densities. (f) Cycling performance of the MnO_2@CC//**1** battery.

space (Fig. 5d). By contrast, the heteromeral carbonyl structure of **2** made water molecules insert into the perinone layers, where only one hydrogen bond exists between each hydroxyl group and water molecule (Fig. 5e). Moreover, free H_2O molecules expand the *d* spacing of the (100) planes from 11.3 Å to 15.1 Å in protonated **2**, resulting in unit cell volume expansion from 861 $Å^3$ to 1182 $Å^3$ (Fig. 5f).

XRD patterns of electrodes from **1** and **2** were collected after 50 cycles. There is no obvious peak displacement for **1**, suggesting that the unit cell remains practically unaffected after cycling (Fig. S37a). In contrast to **1**, the (100) peak of **2** undergoes a small shift relative to that of the pristine one (Fig. S37b). When combined with the results from theoretical calculations, the irreversible displacement of the (100) peak of **2** can be attributed to the expansion of the *d* spacing and therefore lattice expansion caused by the insertion of the large hydrated protons, $H^+{\cdot}(H_2O)_3$. SEM images revealed an elongated cudgel morphology of **2** after 50 and 5000 cycles, which stands in sharp contrast to the unchanged morphology of **1** (Fig. S37c and d). We conclude that an irreversible lattice expansion caused by the larger carrier insertion is the main cause for the less stable charge–discharge profiles and the potential shift of **2**. The results also suggested that the redox reaction would be affected by the local environment of the active sites, including the lattice and the molecular packing.

Electrochemical performance of *cis*-perinone full cells

Encouraged by the impressive stability and fast kinetics of the electrode from **1**, two types of full cells were fabricated using predeposited manganese dioxide on carbon cloth (MnO_2@CC) and activated carbon (AC) as cathodes (Fig. 6a). A mixed solution of 0.5 M H_2SO_4 and 2 M $MnSO_4$, and 0.5 M H_2SO_4 were chosen as electrolytes for the MnO_2@CC//**1** cell and AC//**1** cell, respectively. The morphology of the CC before/after depositing MnO_2 at different times was first monitored by SEM-EDS. It was found that predeposition of 5 mAh MnO_2 was optimal, where a uniform MnO_2 layer was distributed on the carbon cloth (Fig. S38). Due to the near-zero potential of the **1** anode, the MnO_2@CC//**1** battery exhibited a decent voltage of 1.0 V (Fig. 6b and S39). The dQ/dV curve showed that two pairs of redox peaks appeared during the charge–discharge process, with a low overpotential of 0.1 V, which corresponds well to the electrochemical feature of **1** (Fig. 6c).

At a low current density of 0.1 A g^{-1}, the MnO_2@CC//**1** battery delivered a high reversible capacity of 120 mAh g^{-1} based on the mass of **1**. Impressively, the full cell exhibited high rate with slight polarization enhancement (Fig. 6d and e). Even at large current densities of 4 and 10 A g^{-1}, the MnO_2@CC//**1** battery still maintained a capacity of 107 and 100 mAh g^{-1}, respectively. The capacity completely recovered once the current was reverted to 0.1 A g^{-1}. Additionally, a long-term cycling test was conducted at 2 A g^{-1}. The MnO_2@CC//**1** battery performed quite well with a high capacity of 110 mAh g^{-1} after 1500 cycles (Fig. 6f and S40). It is worth noting that capacity retention approached 99%, indicating excellent long-term cycling stability. Similarly, excellent cycling performance was also achieved in the AC//**1** cell except for a low working voltage of 0.5 V, where no capacity fading was observed after 4000 cycles (Fig. S41).

Conclusions

This work demonstrates, by employing *cis*-perinone (**1**) and *trans*-perinone (**2**) as novel proton hosts, the effect of isomerism on the proton storage. Distinct crystalline arrangements and spatial variations in carbonyl active sites significantly influence carrier intercalation and crystal-structure stability, giving rise to different electrochemical behaviors for isomers **1** and **2**. Details of mass transfer and structural evolution as deduced by *in situ* EQCM and crystallography suggested that more water molecules were involved in the charge transfer process for isomer **2** relative to **1**, leading to expansion of the lattice. As a result, **2** suffered from deteriorating potential shift, large polarization, and a change in morphology. By contrast, **1** delivered very stable cycling performance, low polarization, and high rate. After 8000 cycles, isomer **1** was found to maintain 100% of the initial capacity, thereby surpassing state-of-the-art organic materials. Various *in situ* and *ex situ* characterization studies verified that the C=O groups are the active site for reversible proton storage in **1**. Moreover, two types of full devices based on **1** anode and MnO_2 or AC cathode also delivered high rate and cycling stability. Our work provides a fresh understanding on the isomerism effect in the field of energy storage and advances the development of high-performance organic batteries.

Author contributions

G. W. and M. W. conceived the project. Q. L. designed and performed the experiments and analyzed the data. Q. L. and Z. T. conducted DFT calculations. J. Z. conducted formal analysis. Q. F. and K. L. offered EQCM resource. E. D. conducted EPR/UV-vis-NIR spectroelectrochemical measurement. Q. L., G. W., M. W., M. A., and P. N. cowrote the manuscript. G. W. and L. C. supervised the project. All authors discussed the results and commented on the manuscript.

Conflicts of interest

The authors declare no conflict of interest.

Data availability

The data supporting this article have been included as part of the supplementary information (SI). Supplementary information: the experimental methods and related measurements, such as the optical and morphological properties of different structures *via* theoretical and experimental characterization, and device performance. See DOI: https://doi.org/10.1039/d5eb00242g.

Acknowledgements

This project is supported by the National Natural Science Foundation of China (Grant No. 22579176), the Hundred Talents Programs of Chinese Academy of Sciences, the Ningbo Major Research and Development Plan Project (2023Z111), and the Ningbo Yongjiang Talent Programme (2022A-091-G).

References

1 Z. Zhu, W. Wang, Y. Yin, Y. Meng, Z. Liu, T. Jiang, Q. Peng, J. Sun and W. Chen, *J. Am. Chem. Soc.*, 2021, **143**, 20302–20308.
2 Z. Tie and Z. Niu, *Angew. Chem., Int. Ed.*, 2020, **59**, 21293–21303.
3 B. Dunn, H. Kamath and J. M. Tarascon, *Science*, 2011, **334**, 928–935.
4 Y. Xu, X. Wu and X. Ji, *Small Struct.*, 2021, **2**, 2000113.
5 H. Guo and C. Zhao, *Small Methods*, 2024, **8**, e2300699.
6 J. Li, H. Yan, C. Xu, Y. Liu, X. Zhang, M. Xia, L. Zhang and J. Sun, *Nano Energy*, 2021, **89**, 106400.
7 X. Dong, Z. Li, D. Luo, K. Huang, H. Dou and X. Zhang, *Adv. Funct. Mater.*, 2023, **33**, 2210473.
8 Y. Lu and J. Chen, *Nat. Rev. Chem.*, 2020, **4**, 127–142.
9 Z. Zhao-Karger, P. Gao, T. Ebert, S. Klyatskaya, Z. Chen, M. Ruben and M. Fichtner, *Adv. Mater.*, 2019, **31**, e1806599.
10 K. W. Nam, H. Kim, Y. Beldjoudi, T. Kwon, D. J. Kim and J. F. Stoddart, *J. Am. Chem. Soc.*, 2020, **142**, 2541–2548.
11 Z. Tie, L. Liu, S. Deng, D. Zhao and Z. Niu, *Angew. Chem., Int. Ed.*, 2020, **59**, 4920–4924.
12 Z. Wu, Q. Liu, P. Yang, H. Chen, Q. Zhang, S. Li, Y. Tang and S. Zhang, *Electrochem. Energy Rev.*, 2022, **5**, 26.
13 S. Zhang, C. Wei and T. Lin, *Innovation Mater.*, 2025, **3**, 100150.
14 Z. Tie, Y. Zhang, J. Zhu, S. Bi and Z. Niu, *J. Am. Chem. Soc.*, 2022, **144**, 10301–10308.
15 Y. Wang, S. Niu, S. Gong, N. Ju, T. Jiang, Y. Wang, X. Zhang, Q. Sun and H. Sun, *Small Methods*, 2024, **8**, e2301301.
16 D. Shen, A. M. Rao, J. Zhou and B. Lu, *Angew. Chem., Int. Ed.*, 2022, **61**, e202201972.
17 C. Peng, G. Ning, J. Sun, G. Zhong, W. Tang, B. Tian, C. Sun, D. Yu, L. Zu, J. Yang, M. Ng, Y. Hu, Y. Yang, M. Armand and K. P. Loh, *Nat. Energy*, 2017, **2**, 17074.
18 M. Shi, P. Das, Z. S. Wu and T. G. Liu, *Adv. Mater.*, 2023, **35**, e2302199.
19 Y. Chen, H. Dai, K. Fan, G. Zhang, M. Tang, Y. Gao, C. Zhang, L. Guan, M. Mao, H. Liu, T. Zhai and C. Wang, *Angew. Chem., Int. Ed.*, 2023, **62**, e202302539.
20 D. Du, Y. Chen, H. Zhang, J. Zhao, L. Jin, W. Ji, H. Huang and S. Pang, *Angew. Chem., Int. Ed.*, 2024, **63**, e202408292.
21 Y. Zhao, N. Xu, M. Ni, Z. Wang, J. Zhu, J. Liu, R. Zhao, H. Zhang, Y. Ma, C. Li and Y. Chen, *Adv. Mater.*, 2023, **35**, e2211152.
22 R. Wang, J. He, C. Yan, R. Jing, Y. Zhao, J. Yang, M. Shi and X. Yan, *Adv. Mater.*, 2024, **36**, 2402681.
23 J. Zhao, Y. Xue, Y. Shen, Y. Teng, C. Sun, W. Ji, H. Huang and S. Pang, *Angew. Chem., Int. Ed.*, 2025, **64**, e202514164.

24 C. Strietzel, M. Sterby, H. Huang, M. Strømme, R. Emanuelsson and M. Sjçdin, *Angew. Chem., Int. Ed.*, 2020, **59**, 9631–9638.
25 X. Liu, Z. Yang, Y. Lu, Z. Tao and J. Chen, *Small Methods*, 2024, **8**, e2300688.
26 C. Huang, W. Zhang and W. Zheng, *Energy Storage Mater.*, 2023, **61**, 102913.
27 Y. Ma, Y. Wei, W. Han, Y. Tong, A. Song, J. Zhang, H. Li, X. Li and J. Yang, *Angew. Chem., Int. Ed.*, 2023, **62**, e202314259.
28 Z. Guo, J. Huang, X. Dong, Y. Xia, L. Yan, Z. Wang and Y. Wang, *Nat. Commun.*, 2020, **11**, 959.
29 X. Yang, Y. Ni, Y. Liu, Q. Zhang, J. Hou, G. Yang, X. Liu, W. Xie, Z. Yan, Q. Zhao and J. Chen, *Angew. Chem., Int. Ed.*, 2022, **61**, e202209642.
30 F. Yue, Z. Tie, S. Deng, S. Wang, M. Yang and Z. Niu, *Angew. Chem., Int. Ed.*, 2021, **60**, 13882–13886.
31 J. Mizuguchi, *J. Phys. Chem. B*, 2004, **108**, 8926–8930.
32 M. Lapkowski, *Materials*, 2021, **14**, 6880.
33 L. Tapmeyer, M. Bolte, M. R. Chierotti and M. U. Schmidt, *Dyes Pigm.*, 2020, **181**, 108442.
34 M. J. Taublaender, F. Glocklhofer and M. Marchetti-Deschmann, *Angew. Chem., Int. Ed.*, 2018, **57**, 12270–12274.
35 M. Mamada, C. Perez-Bolivar, D. Kumaki, N. Esipenko, S. Tokito and P. Anzenbacher, *Chem. – Eur. J.*, 2014, **20**, 11835–11846.
36 M. Wang, S. Fu, P. Petkov, Y. Fu, Z. Zhang, Y. Liu, G. Chen, S. Gali, L. Gao, Y. Lu, S. Paasch, H. Zhong, H. Steinrück, E. Cánovas, E. Brunneer, D. Beljonne, M. Bonn, H. Wang, R. Dong and X. Feng, *Nat. Mater.*, 2023, **22**, 880–887.
37 M. Wang, G. Wang, C. Naisa, Y. Fu, S. Gadi, C. Paasch, E. Brunner, S. Zhou, D. Beljonne, H. Steinrück, R. Dong and X. Feng, *Angew. Chem., Int. Ed.*, 2023, **62**, e202310937.
38 T. Ma, Y. Yang, D. Johnson, K. Hansen, S. Xiang, R. Thakur, A. Djire and J. Lutkenhaus, *Joule*, 2023, **7**, 2261–2273.
39 J. He, M. Shi, H. Wang, H. Liu, J. Yang, C. Yan, J. Zhao, J. Yang and X. Wu, *Angew. Chem., Int. Ed.*, 2024, **63**, e202410568.
40 V. L. Murphy and B. Kahr, *J. Am. Chem. Soc.*, 2011, **133**, 12918–12921.
41 H. Dai, Y. Chen, Y. Cao, M. Fu, L. Guan, G. Zhang, L. Gong, M. Tang, K. Fan and C. Wang, *Nano-Micro Lett.*, 2023, **16**, 13.
42 M. Yang, Y. Hao, B. Wang, Y. Wang, L. Zheng, R. Li, H. Ma, X. Wang, X. Jing, H. Li, M. Li, Z. Wang, Y. Dai, G. Shan, M. Hu, J. Luo and J. Yang, *Natl. Sci. Rev.*, 2024, **11**, nwae045.
43 X. Wang, Y. Wada, T. Shimada, A. Kosaka, K. Adachi, D. Hashizume, K. Yazawa, H. Uekusa, Y. Shoji, T. Fukushima, M. Kawano and Y. Murakami, *J. Am. Chem. Soc.*, 2024, **146**, 1832–1838.
44 C. Li, L. Hu, X. Ren, L. Lin, C. Zhan, Q. Weng, X. Sun and X. Yu, *Adv. Funct. Mater.*, 2024, **34**, 2313241.
45 V. Kumar, H. Bharathkumar, S. D. Dongre, R. Gonnade, K. Krishnamoorthy and S. S. Babu, *Angew. Chem., Int. Ed.*, 2023, **62**, e202311657.
46 D. A. Zherebtsov, M. U. Schmidt, R. Niewa, C. P. Sakthidharan, F. V. Podgornov, Y. V. Matveychuk, S. A. Nayfert and F. Guo, *Acta Crystallogr.*, 2019, **75**, 384–392.
47 J. Z. Mizuguchi, *Kristallogr. – New Cryst. Struct.*, 2003, **218**, 137–138.
48 J. Z. Mizuguchi, *Kristallogr. – New Cryst. Struct.*, 2003, **218**, 139–140.
49 X. Wang, C. Bommier, Z. Jian, Z. Li, R. Chandrabose, I. Rodrguez-Perez, P. Greaney and X. Ji, *Angew. Chem., Int. Ed.*, 2017, **56**, 2909–2913.
50 G. Zhao, X. Yan, Y. Dai, J. Xiong, Q. Zhao, X. Wang, H. Yu, J. Gao, N. Zhang, M. Hu and J. Yang, *Small*, 2024, **20**, e2306071.
51 Z. Tie, S. Deng, H. Cao, M. Yao, M. Yao, Z. Niu and J. Chen, *Angew. Chem., Int. Ed.*, 2022, **61**, e202115180.
52 W. Han, M. Li, Y. Ma and J. Yang, *Electrochim. Acta*, 2022, 403.
53 X. Wang, J. Zhou and W. Tang, *Energy Storage Mater.*, 2021, **36**, 1–9.
54 K. C. S. Lakshmi, B. Vedhanarayanan, H. Cheng, X. Ji, H. Shen and T. Lin, *J. Colloid Interface Sci.*, 2022, **619**, 123–131.
55 T. Sun, H. Du, S. Zheng, J. Shi, X. Yuan, L. Li and Z. Tao, *Small Methods*, 2021, **5**, e2100367.
56 M. Zhu, L. Zhao, Q. Ran, Y. Zhang, R. Peng, G. Lu, X. Jia, D. Chao and C. Wang, *Adv. Sci.*, 2022, **9**, e2103896.
57 M. Frisch, G. Trucks, H. Schlegel, G. Scuseria, M. Robb, J. Cheeseman, G. Scalmani, V. Barone, G. Petersson and H. Nakatsuji, *Gaussian 16, Revision A. 03*, Gaussian, Inc., Wallingford CT, 2016.
58 T. Lu and F. Chen, *J. Comput. Chem.*, 2012, **33**, 580–592.
59 Y. Ji, Z. Yin, Z. Yang, Y. Deng, H. Chen, C. Lin, L. Yang, K. Yang, M. Zhang, Q. Xiao, J. Li, Z. Chen, S. Sun and F. Pan, *Chem. Soc. Rev.*, 2021, **50**, 10743–10763.
60 C. P. Grey and J. M. Tarascon, *Nat. Mater.*, 2016, **16**, 45–56.
61 T. Ma, C. H. Li, R. M. Thakur, D. P. Tabor and J. L. Lutkenhaus, *Nat. Mater.*, 2023, **22**, 495–502.
62 S. Wang, F. Li, A. D. Easley and J. L. Lutkenhaus, *Nat. Mater.*, 2019, **8**, 69–75.
63 K. Xu, T. Ruoko, M. Shokrani, D. Scheunemann, H. Abdalla, H. Sun, C. Yang, Y. Puttisong, N. B. Kolhe, J. S. M. F. Figueroa, T. Ederth, W. M. Chen, M. Berggren, S. A. Jenekhe, D. Fazzi, M. Kererink and S. Fabiano, *Adv. Funct. Mater.*, 2022, **32**, 2112276.
64 O. Unsalan, Y. Sert, C. Altunayar-Unsalan and S. Erten-Ela, *Spectrochim. Acta, Part A*, 2023, **294**, 122516.